Cells interpret temporal information from TGF-β through a nested relay mechanism

Jingyu Zhang[1✦], Xiao-Jun Tian[1✦], Yi-Jiun Chen[1], Weikang Wang[1], Simon Watkins[2], and Jianhua Xing[1]*

[1]Department of Computational and Systems Biology, School of Medicine, University of Pittsburgh, Pittsburgh, PA, 15260, USA

[2]Department of Cell Biology, School of Medicine, University of Pittsburgh, Pittsburgh, PA, 15260, USA

✦ The two contributed equally.

*To whom correspondence should be sent: xing1@pitt.edu

Abstract

The detection and transmission of the strength and temporal quality of intracellular and extracellullar signals is an essential cellular mechanism. While TGF-β signaling is one of the most thoroughly studied signaling pathways, the mechanisms by which cells translate TGF-β signals remain unclear. In this paper, through an integrated quantitative and computational approach we demonstrate that crosstalk among multiple TGF-β activated pathways forms a relay from SMAD to GLI1 that initializes and maintains SNAILl expression, respectively. This transaction is smoothed and accelerated by another temporal switch from elevated cytosolic GSK3 enzymatic activity to reduced nuclear GSK3 enzymatic activity. This nested relay mechanism places SNAIL1 as a key integrator of information from TGF-β signaling subsequently distributed through divergent pathways; essentially cells generate a transient or

sustained expression of SNAIL1 depending on TGF-β duration. Our results provide a mechanistic understanding of a long-standing paradox that TGF-β can both suppress and promote cancer development.

.

Keywords: TGF-β, SNAIL1, GLI code, GSK3, information flow,

Introduction

Cells live in as state of constant environmental flux and must reliably receive, decode, integrate and transmit information from extracellular signals such that response is appropriate [1-4]. Dysregulation of signal transduction networks leads to inappropriate transmission of signaling information which may ultimately lead to pathologies such as cancer. Therefore a central problem in systems biology has been to untangle how cellular signal mechanisms are encoded and decoded.

Cellular responses may have distinct temporal profiles. An adaptive response is transient, and the system generally returns to the pre-stimulation state. An inflammatory response is a classical example of this, where multiple levels of negative feedback and incoherent feed-forward loops ensure final resolution and prevent chronic inflammatory responses [5]. In contrast a sustained response may persist after removal of the original signal – typically through positive feedback loops. Some cellular signals affect multiple cellular processes through a number of pathways and induce both types of responses under different circumstances. However it remains an open question as to how cells decide, generate and inter-convert between these different forms of responses.

One example of multifunctional factor is the transforming growth factor-β (TGF-β), a secreted protein that regulates both transient and persistent cellular processes such as proliferation, morphogenesis, homeostasis, differentiation, and the epithelial-to-mesenchymal transition (EMT) [6-10]. The multifunctional roles of TGF-β have challenged the central paradigm in endocrinology that each hormone has a single functional role. Since its discovery in 1980s [11], researchers have been puzzled by the enigma of "how cells read TGF-β signals", arising from seemingly

paradoxical observations seen when TGF-β acts as both inhibitor of pre-malignant cells and promoter of invasion and metastasis in the later stage of tumor development [6, 7]. Because it plays essential roles in developmental and normal physiological process, and its dysregulation is related to cancer, fibrosis, inflammation, Alzheimer's disease and many other diseases, the TGF-β signaling pathway has been probed extensively as a potential pharmaceutical target [12, 13]. However, this is difficult to do without understanding the seemingly dichotomous roles of TGF-β.

To dissect this enigma we focused on one facet of this process: TGF-β induced SNAIL1 expression. SNAIL1 is a target of TGF-β signaling and plays a key role in regulating a number of subsequent downstream processes. While most existing quantitative studies focus on the TGF-β-SMAD axis [14-16], our results show that crosstalk between the SMAD-dependent and independent pathways are key to understanding how cells decode and transmit temporal and contextual information from TGF-β. We posit that the mechanism may be a central mechanistic signal transduction process as many signaling pathways share the network structure.

Results

The canonical TGF-β/SMAD/SNAIL1 pathway cannot explain two waves in SNAIL1 dynamics.

Most existing knowledge as to how cells interpret TGF-β signals resides in the canonical TGF-β pathway, where TGF-β leads to phosphorylation of SMAD2 and SMAD3 (pSMAD2/3), followed by nuclear entry and action as a direct transcription factor for multiple downstream genes [16, 17]. Among the regulatory targets of pSMAD2/3 is activation of its own inhibitor, I-SMAD. pSMAD2/3 and I-SMAD create a negative feedback loop, which leads to only a

transient localization of pSMAD2/3 in the nucleus. pSMAD2/3 also promotes expression of SNAIL1. Due to the double-negative feedback loops between SNAIL1 and miR-34 family proteins, the expression of SNAIL1 is sustained after decay of nuclear pSMAD2/3. This mechanism is supported by SMAD2/3 binding sites on the promoter region of snail1 [18].

Since quantifying SMAD proteins are the fundamental readouts of most current TGF-β signaling studies, we set out to examine the downstream localization and abundance of SNAIL directly. Human MCF10A cells were treated with recombinant TGF-β1 and multicolor immunofluorescence (IF) was performed using antibodies directed against pSMAD2/3, SNAIL1. As expected pSMAD2/3 proteins accumulated in the nucleus transiently, peaking at 12 hours after TGF-β1 treatment, followed by a decrease by 24 hours (Fig. 1B & C). We confirmed the transient pSMAD2/3 dynamics by sampling 1100-2600 cells at each time point (Fig. 1C). The result is consistent with reports in the literature [14, 16, 19], and supports the theoretical prediction of a negative feedback loop. Interestingly SNAIL1expression showed an additional twist to the theoretical prediction of a sustained response. In our experiments nuclear SNAIL1 concentration rose concurrently with pSMAD2/3 (Fig. 1B & C), then there was a surprising and transient dip at 24 hours, followed by another increase followed by a persistant elevation for one week [20]. Importantly this is not cell type dependent as equivalent two-wave dynamics were seen for *SNAIL1* mRNA in MCF10A (Fig. 1D), MCF7 and A549 cells (Fig S1B), suggesting there may be a secondary activator of SNAIL1.

To address the hypothesis that the activation of SNAIL1 is multifactorial and not solely dependent on SMAD2/3 we treated MCF10A cells with a SMAD2/3 inhibitor LY2109761 in addition to TGF-β treatment (Fig. 1D). When the inhibitor was added concurrently with TGF-β treatment, the *SNAIL1* mRNA level was reduced to ~ 9% of that of the control (no inhibitor)

experiment by day 3, indicating that indeed pSMAD2/3 are required for SNAIL1 activation. However, the *SNAIL1* mRNA level remained ~ 70% when the inhibitor was added 48 hours after initiation of TGF-β treatment (when nuclear pSMAD2/3 concentration has dropped to a minimum). Equivalent effects were seen with MCF7 and A549 cells (Fig. S1C). These results reveal that pSMAD2/3 is essential for the early phase of SNAIL1 activation, but is less important for the secondary phase elevation and persistence of SNAIL1 expression/localization.

One possible explanation is that the double-negative feedback loop between miR-34 and SNAIL1 may reactivate SNAIL1 expression at day 2. However, our quantitative PCR measurements revealed that reduction of miR-34 expression took place after day 2 ruling out this possibility (Fig. S1D). Furthermore we performed a thorough parameter space search using a multi-configuration Monte Carlo algorithm (Fig. S1E) over a mathematical model for the network in Fig. 1A. The search revealed regions of the parameter space that quantitatively reproduced the transient pSMAD2/3 dynamics, but not the two-wave dynamics of SNAIL1 expression (Fig. 1E). Therefore both experimental results and computational analysis strongly suggest that the accepted mechanism shown in Fig. 1A is in fact incomplete, and there are one or more missing links between TGF-β and SNAIL1.

GLI1 is a signaling connector between SMAD and SNAIL1.

Subsequently we performed network analysis and showed that SMAD-dependent and -independent pathways may form a highly connected TGF-β signaling network (Fig. S2A), in common with previous reports [21]. Our analysis identified GLI1, a key component of the Hedgehog pathway, as a signaling hub in the network (Fig. 2A). TGF-β treatment can lead to elevated GLI1 expression, either through transcriptional activation by pSMAD2/3, or through degrading GSK3, while the latter facilitates GLI1 and SNAIL1 protein degradation [22, 23]. The

network integrates multiple feed-forward loops that converge at the regulation of SNAIL1 transcription. We therefore hypothesized that at the point when the SMAD ceases to function as a major transcription factor of SNAIL1, it has already induced GLI1 expression, and that the concentration of GLI1 may be sustained through positive feedback and continued induction via other impactful TGF-β signaling pathways. Essentially, a relay from pSMAD2/3 to GLI1 initiates and then maintains SNAIL1 expression.

To test this hypothesis, we performed microscopy studies of SNAIL1-GLI1 using MCF10A cells. The distribution of SNAIL1 found in this study (Fig. S2B) was consistent with those from the pSMAD2/3-SNAIL1 studies. Elevated and sustained expression of GLI1 under TGF-β treatment (Fig. 2B & C) was clearly evident. More interestingly GLI1 also showed an unexpected multi-phasic dynamic. Around 8 hours after TGF-β treatment, cytosolic GLI1 concentration started to increase. At 12 hours when SMAD activities decreased toward basal levels there was a clear accumulation of GLI1 in the nucleus, which continued to increase through day 2. Notably, at this time point cells expressing a high level of nuclear SNAIL1 consistently showed high intranuclear concentrations GLI1 (Fig. S2B), strongly suggesting that the second wave of SNAIL1 is caused by sustained GLI1 expression. Computational modeling of the network in Fig. 2A also reproduced the temporal dynamics of pSAMD2/3 and SNAIL1 (Figure S2C).

If GLI1 is involved in the maintenance of SNAIL1 expression subsequent to the drop in pSMAD2/3 concentration, it is reasonable to predict (Fig. S2D) that inhibiting GLI1 activity, either at the onset of or at some subsequent time after TGF-β treatment, would have minimal effect on the initial wave of SNAIL1 expression since it is caused by pSMAD2/3. However, it would eliminate the second wave of SNAIL1 expression. Indeed this was observed when the GLI1 inhibitor GANT61 was added together with TGF-β at the beginning of the experiment

resulting in a reduction of the *SNAIL1* mRNA level to be 55% (at 12 h and 24 h), 12% (at 48 h) and 7% (at 72 h) compared to those without inhibition at the corresponding time points. In another experiment adding the inhibitor 48 hours after TGF-β treatment also reduced the mRNA level measured at 72 h to be 25% (Fig. 2D). These results are qualitatively different from those with the SMAD inhibitor (Fig. 1D).

To confirm that GLI1 activation is not restricted to the MCF10A cell line, we also examined MCF7 and A549 cells with TGF-β treatment, and observed similar increased and sustained GLI1 expression (Fig. S2E). Furthermore, early and late GLI1 inhibition lead to a reduction of the *SNAIL1* mRNA level to be 13% and 22% for MCF7 cells, and to a less extent of 57% and 66% for A549 cells, respectively (Fig. S2F). Additionally, increased GLI1 expression after TGF-β treatment has been found for multiple liver cancer cell lines [24]. *In toto* these results support the potential role of GLI1 as a signaling relay from pSMAD2/3 to SNAIL1.

GSK3 in a phosphorylation form with augmented enzymatic activity accumulates at endoplasmic reticulum and Golgi apparatus.

Next, we hypothesized that GSK3 is fundamental to the observed multi-phasic GLI1 dynamic (Fig. 2). Most published studies suggest that GSK3 is constitutively active in untreated cells, facilitating degradation of SNAIL1 and GLI1; TGF-β treatment leads to GSK3 phosphorylation and inactivation, which leads to an accumulation of SNAIL1 and GLI1 [25, 26].

Initially we tested whether the above mechanism is sufficient to explain the multi-phasic GLI1 dynamics. We treated MCF10A cells in the absence of TGF-β with a GSK3 inhibitor that suppresses GSK activity without interfering with its phosphorylation. Given the above mechanism, one should expect the GSK3 inhibitor to promote both GLI1 and SNAIL1. In our experiment, SNAIL1 did increase, but there was no change in GLI1 expression in either nucleus

or cytoplasm (Fig. 3A), suggesting additional signaling mechanisms may be involved.

Besides the inhibitory serine phosphorylation, the literature suggests that tyrosine (Y279 in GSK-3α and Y216 in GSK-3β) phosphorylation leads to augmented enzymatic activity of GSK3 [27]. As a convenience when discussing the three forms of GSK3, we refer the enzymatically active unphosphorylated form and the more active tyrosine phosphorylated form as "$GSK3^{A}$" and "$GSK3^{AA}$", respectively, and the inactive serine phosphorylation form as "$GSK3^{D}$". Also we reserve "GSK3" for the total GSK3. As expected, microscopy studies showed an increased concentration of $GSK3^{D}$ peaking around 12 hours after TGF-β treatment (Fig. 3B, Fig. S3A). Large cell-to-cell variations in the concentration of $GSK3^{D}$ were observed, however, the abundance of cytosolic and nuclear $GSK3^{D}$ were essentially equivalent (the expression ratio was close to one) for cells without TGF-β treatment (Fig. S3B). This observation corroborates earlier report that the serine phosphorylation does not affect GSK3 nuclear location [28]. TGF-β treatment led to transient deviation of this ratio from equivalence, reflecting additional active and dynamic regulation of GSK3 including covalent modification, location and protein stability. Specifically prior to inhibitory serine phosphorylation we observed transient $GSK3^{AA}$ accumulation in the perinuclear region peaking at eight hours (Fig. 3B, Fig. S3A). Close examination of higher magnification confocal images revealed that the $GSK3^{AA}$ formed clusters in the endoplasmic reticulum (ER) and Golgi apparatus, but not associated with actin filaments (Fig. 3C, Movie 1 & 2). Given that a function of active GSK3 is to modify target proteins post-translationally, our observation suggests an unreported role for $GSK3^{AA}$ accumulating at the ER and Golgi apparatus is to modify newly synthesized proteins before their release to the cytosol. Specifically previous studies showed that in mammalian cells a scaffold protein SUFU binds to GLI to form an inhibitory complex, and SUFU phosphorylation by GSK3β prevents the complex formation,

exposes the GLI1 nuclear localization sequence [29], which explains the observed increase of free GLI1 in the cytosol followed by nuclear translocation (Fig. 2B). Since the two phosphorylation forms, $GSK3^{AA}$ and $GSK3^{D}$, coexist within single cells at defined time points, we performed co-immunoprecipitation and found that the probability of having the two GSK3 phosphorylation forms in one molecule was undetectable (Fig. S3C).

Contrary to our observation that TGF-β regulates $GSK3^{AA}$ dynamics, other studies posit that $GSK3^{AA}$ is not regulated by external cues [30]. To resolve this paradox, we measured the relative amount of different GSK3 forms through silver staining (Fig. S3D). Among the three forms, the overall percentage of $GSK3^{D}$ increased from a basal level of 37% to 65% at 12 h after TGF-β treatment. In contrast, only a small fraction of GSK3 molecules assumed the $GSK3^{AA}$ form and its overall abundance was stable over time (from ~10% basal level to ~13% at 8 h then back to ~10% at 12 h after TGF-β treatment). Essentially levels of $GSK3^{AA}$ did not change in abundance but did change in localizations (homing to the ER and Golgi apparatus) to form a high local concentration, which imbue an important role in TGF-β signaling.

A temporal and compartment switch from active to inhibitory GSK3 phosphorylation smooths the SMAD-GLI1 relay and reduces cell-to-cell heterogeneity on GLI1 activation.

Based on the above results, we constructed an expanded network for TGF-β induced SNAIL1 expression, which integrates a role for GSK3 and its switching among the three phosphorylation forms as well as a functional role due to its intracellular redistribution (Fig. 4A). The model reproduces the multiphasic dynamics of GLI1 as well as that of pSMAD2/3 and SNAIL1 (Fig. S4A).

To understand the function of the early nuclear accumulation of GLI1 induced by $GSK3^{AA}$, it is important to recognize that GLI1 has a positive-feedback loop, and this network motif (Fig. 4B,

left panel) has characteristic sigmoidal shaped temporal dynamics, with the substrate concentration increasing slowly at first then accelerating with time until it approaches saturation (Fig. 4B, right panel, red curve). The response time, t_R, defined as the time taken to reach a target concentration value $[X]_R$, is highly sensitive to initial substrate concentration $[X]_0$: in fact a slight increase in the initial concentration, $\Delta[X]$, will significantly shorten response time (Fig. 4B, right panel, blue curve), and for a fixed $\Delta[X]$ a greater acceleration is seen in cells with lower initial concentrations (Fig. 4B, right panel, inlet figure). Consequently despite variations of their initial concentration of X, most cells within a population can reach $[X]_R$ by a targeted time point t_T in a series of temporally regulated events such as cell differentiation and immune response. The needed concentration boost may be effected by conversion of preformed molecules from an inactive form into an active form (Fig. 4B, left panel, the part of the network in green). Indeed, many examples of this modified feedback loop motif exist. Figure S4B gives some examples involving members of intrinsically disordered proteins and inhibitors of DNA binding proteins, β-catenin and the STING motif for immune responses. In the present scenario the accelerated GLI1 dynamic ensures sufficient accumulation of GLI1 before nuclear pSMAD2/3 level decreases, essentially analogous to a relay race when the first runner can only release the baton after the second runner has grabbed it. Later when the GLI1 and SNAIL1 concentrations start to increase, the $GSK3^A \rightarrow GSK3^D$ conversion became necessary to reduce the rates of their degradation catalyzed by active GSK3. Interestingly, this conversion takes place concurrently with maximal concentration of nuclear pSMAD2/3, which activates GLI1 and SNAIL1 transcription. Furthermore, the small initial concentration boost does not affect another major function of the positive feedback loop, which is to robustly buffer fluctuations in signal strengths via bistable dynamics (Fig. S4C).

To test the functional roles of GSK3 suggested above, we performed a series of GSK3 activity inhibition experiments. First, we pretreated MCF10A cells with GSK3 inhibitor SB216763, washed out the inhibitor then added TGF-β1 (Fig. S4B). We predicted that the treatment would slow down GLI1 nuclear accumulation, and at later times decrease the overall increase of GLI1 and SNAIL1 compared to cells without GSK3 inhibitor. Indeed this was observed (Fig. 4C, TGF-β +/- GSK3_I). More interestingly, the scatter plots show the distributions with and without the inhibitor are similar in cells with high GLI1, but in the presence of inhibitor there is a population of non-responsive cells with low GLI1 and SNAIL1. This observation is consistent with the model prediction that the GSK3-induced boost of initial GLI1 concentration leads an acceleration in the response time for cells with lower initial nuclear GLI1 concentration (Fig. 4B, right panel). In a separate experiment (Fig. S4C), we did not wash out GSK3 inhibitor while adding TGF-β. In this case the inhibitor had opposite effects on the GLI1/SNAIL1 protein concentration: it slowed down the initial release and translocation of GLI1 needed to accelerate the GLI1 accumulation, but also decreased GLI1 and SNAIL1 degradation that becomes pre-eminent when the proteins were present at high levels. Compared to the samples grown in the absence of the GSK3 inhibitor, we also observed slower and more scattered GLI1 nuclear accumulation and SNAIL1 increase on day 2, but by day 3 the overall levels of GLI1 and SNAIL1 were actually higher than the case without the inhibitor (Fig. 4C, TGF-β + GSK3_I).

The SMAD-GLI1 relay increases the network information capacity and leads to differential response to TGF-β duration

Our results show that TGF-β1 signaling is effected through pSMAD2/3 directly with fast pulsed dynamics concurrently with a relay through GLI1 which has a much slower dynamics. The signaling ported by these two channels converges on SNAIL1 with a resultant two-wave

expression pattern. To further dissect the potential functional interactions between these two pathways, we performed mathematical modeling and predicted that the two distinct dynamics allows cells to respond to TGF-β differentially depending on stimulus duration (Fig. 5A). Short pulses of TGF-β only activate pSMAD2/3 and the first wave of transient SNAIL1 expression. When the signal duration is longer than a defined threshold value, activation of GLI1 will lead to the observed second wave of SNAIL1 expression. We confirmed the predictions with MCF10A cells (Fig. 5B). Both TGF-β1 pulses with duration of two hours and eight hours activated pSMAD2/3 and the first wave of SNAIL1 expressions. However, only the eight-hour but not the two-hour pulse activated sustained GLI1 and the second wave of SNAIL1 expression, similar to those with continuous TGF-β1 treatment.

Clearly cellular responses have different temporal profiles depending on the TGF-β duration, and one can use the information theory to quantify their information content [31, 32]. In this study we utilized a more intuitive understanding of network function from an information encoding viewpoint. Consider the pSMAD complex, which has three coarse-grained states, High (H), Medium (M), and Low (L), and each of GLI1 and SNAIL1 has two states, H and L (Fig. 5C). Then one can use three 4-element states, (L, L; L, L), (H, L; L, L), (H, M; L, H) to roughly describe the case without TGF-β and the 8 hour and 12 hour pulse results in Fig. 5B, where each number in a state represents in the order the 12 h and 48 h concentrations of pSMAD2/3 and GLI1, respectively. The three states are part of a temporally ordered state space, and encode information of TGF-β duration roughly as not detectable, short, and long. The same information is encoded by the SNAIL1 dynamics as (L, L), (H, L), and (H, H), reflecting SNAIL1 as an information integrator of the two converging pathways.

Further modeling suggests that components in the network function cooperatively to encode the TGF-β information (Fig. S5A). Increasing or decreasing the nuclear GSK3 enzymatic activity tunes the system to generate the second SNAIL1 wave with a higher or lower threshold of TGF-β duration, respectively, while changing the cytosol GSK3 enzymatic activity has the opposite effect. Upregulation of GLI1, or downregulation of I-SMAD, both of which have been observed in various cancer cells, also decrease the threshold for generating the second SNAIL1 wave. Therefore cells of different types can share the same network structure, but fine-tune their context-dependent responses by varying some dynamic parameters, and for a specific type of cells dysregulation of any of the signaling network components may lead to misinterpretation of the quantitative information of TGF-β signal.

Discussion

TGF-β is a multifunctional cytokine that can induce a plethora of different and mutually exclusive cellular responses. Despite the growing number of studies related to TGF-β signaling, it remains enigmatic how cells interpret the signal. It is suggested that one factor contributing to this complexity comes from the fact that TGF-β can activate a number of pathways interconnected with multiple crosstalk points. Our studies reveal that this interconnection is essential such that components of the network can function coordinately and appropriately to interpret the temporal (time and duration) information from TGF-β.

pSMADs are major inducers for the first wave of SNAIL1 expression.

The two-wave dynamic of TGF-β-induced SNAIL1 expression has been observed in several cellular systems [21, 33], supporting the underlying relay mechanism discovered in this work. The first wave is fundamentally induced by pSMAD2/3, as evidenced from our SMAD inhibition

experiments, and similarity between the dynamics of pSMAD2/3 and the first wave of SNAIL1. SNAIL1 may act as cofactor of pSMADs to induce other early response genes [34]. At later times the nuclear concentrations of pSMAD2/3 decrease though continue to contribute to SNAIL1 activation at a lower level.

GLI1 is a signaling hub for multiple pathways and temporal checkpoint for activating second-wave of sustained SNAIL1 expression.

GLI protein has been traditionally attributed to the canonical Hedgehog pathway. Here we show that TGF-β induction of GLI1 relays the signal to induce SNAIL1. Consistent with the present study, Dennler et al. reported SMAD3-dependent induction of the GLI family by TGF-β both in multiple cultured cell lines, and in transgenic mice overexpressing TGF-β [22] Many other signals such as PGF, EGF can also activate the GLI family, and a GLI code has been proposed to integrate input from different pathways and lead to context-dependent differential responses [35]. Our results confirmed this role of GLI1 as an intermediate information integrator and transmitter, and suggest that both the strength and duration of the TGF-β stimulation are important, and must act above threshold concentrations and durations to activate the second wave of SNAIL1. This temporal and strength checkpoint prevents spurious SNAIL1 activation and subsequent major cellular fate changes.

GSK3 fine-tunes the threshold of the GLI1 checkpoint and synchronizes responses of a population of cells

The functional switch from pSMAD2/3 to GLI1 relays information from TGF-β signaling beyond the initial induction of SNAIL1, and this relay is facilitated by a second relay from the active to the inactive phosphorylation form of GSK3 proteins. Active regulation of the abundance and nuclear location of $GSK3^{AA}$ form has been observed in neurons [36]. In contrast to

these earlier reports we observed an accumulation of $GSK3^{AA}$ in the ER and Golgi apparatus. Mechanistically this may be caused by redistribution of cytosolic $GSK3^{AA}$, or a simple accumulation of *de novo* synthesized and phosphorylated GSK3 proteins. The overall consequence is an increase in local GSK3 enzymatic activity, which forms part of the GSK3 switch that smooths the pSMAD2/3-GLI1 transition and the duration threshold of TGF-β pulse that generates the second wave of SNAIL1.

This seemingly simple process, which accelerates the response time through transient and minor increases in the initial concentration of a molecular species subject to positive feedback control, may have profound biological functions. Positive feedback loops are ubiquitous in cellular regulation, with a major function to filter both the strength and temporal fluctuations of stimulating signals and to prevent inadvertent cell fate change. This network, however, may have an inherently slow response time, and the response is highly sensitive to initial conditions that lead to large cell-to-cell variation of temporal dynamics. This variation and slow dynamic may be problematic for processes such as neural crest formation and wound healing where precise and synchronized temporal control is crucial for generating collective responses of multiple cells. Transient increases in initial protein concentrations of the GSK3 module may solve the seemingly incompatible requirements for the motif on robustness against fluctuations as well as fast and synchronized responses. It assures that despite a possible broad distribution of basal expression levels of the protein, cells are activated within a designated period of time at the presence of persistent activation signal, without scarifying the filtering function of the feedback loop.

Cells use a temporally ordered state space formed by a composite network to increase information transfer capacity.

Cells constantly encounter TGF-β signals with different strengths and duration, and must respond accordingly. It is well documented that biological networks reliably transmit information about the extracellular environment despite intrinsic and extrinsic noise in a subtle and functional way. However, quantitative analyses using information theory reveal that the dynamic of each individual readout is quite coarse with one or few bits [31, 32]. This is a paradox. However, our results suggest that cells use multiple readouts to generate a temporally ordered state space with an expanded capacity to encode signal information and generate a far more subtle response system. For example, the SMAD motif has a refractory period due to the negative feedback loop and thus can accurately encode the duration information of TGF-β only within a limited temporal range, then the GLI1 motif encodes information of longer TGF-β duration which then saturates. This temporally ordered state network may be further expanded, such that the SNAIL1 motif itself possibly encodes information of longer TGF-β duration and relays to other transcription factors such as TWIST and ZEB, and lead to stepwise transition from the epithelial to the mesenchymal phenotype depending on the TGF-β duration [20].

As with other signaling process, TGF-β signaling is context dependent, and the dynamic and regulatory network vary between cell types [15, 37]. For the three cell lines we examined our results identify GLI1 as a major relaying factor for the TGF-β signaling. The inhibition experiments show that other possible peripheral links have minor contributions to SNAIL1 activation, while their weights may grow at time later than we examined. Consequently the present work has focused on the early event of TGF-β activation of SNAIL1, which is with 72 h for MCF10A cells. Nevertheless, the relay mechanism and the corresponding network structure identified here can be general for transmitting quantitative information of TGF-β and other signals. It is typical that an extracellular signal is transmitted through a canonical pathway with negative feedbacks

and multiple non-canonical pathways, and these pathways crosstalk at multiple points, and Fig. S5B gives some examples including IL-12, DNA double strand breaking, and LPS. Therefore the mechanism revealed in this work is likely beyond TGF-β signaling.

Abnormal upregulation of GLI1 dysregulates SNAIL1 activation and changes TGF-β from tumor suppressor to metastasis promoter.

Returning to the TGF-β paradox mentioned in the introduction. Our results revealed a network which integrates several factors that work cooperatively to interpret the temporal information of TGF-β and generate distinct SNAIL1 expression patterns. Franco et al. showed that SNAIL1 suppresses TGF-β induced apoptosis and promotes [38]. In premalignant cells such as MCF10A cells GLI1 still functions close to normal as a temporal checkpoint of TGF-β on inducing SNAIL1 activation, thus TGF-β serves as a tumor suppressor by inducing apoptosis through the SMAD-dependent pathway. On the other hand, GLI1 is upregulated in many types of cancer and the MCF7 and A549 cells we studied (28), so under TGF-β stimulation these cancer cells are prone to SNAIL1 activation and EMT instead of apoptosis.

Network temporal dynamics is a key for effective pharmaceutical intervention.

Upregulation of GLI1, and GSK3 and the responsive SMAD family has been reported in pathological tissues of fibrosis [39]and cancer [35], and all three have been considered as potential drug targets. The present study emphasizes that in cell signaling timing is fundamental to function. The same network structure may generate drastically different dynamics with different parameters, as observed for different cell types. Consequently, effective biomedical intervention needs to take into account the network dynamics. We have already demonstrated that adding the inhibitors at different stages of TGF-β induction can be either effective versus not effective on reducing SNAIL1 (by inhibiting pSMAD2/3), both effective (by inhibiting GLI1), and even

opposite (by inhibiting GSK3). Actually, one may even exploit this dynamic specificity for precisely targeting certain group of cells while reducing undesired side effects on other cell types.

In summary through integrated quantitative measurements and mathematical modeling we provided a mechanistic explanation for the long-time puzzle of how cells read TGF-β signals. Several uncovered specific mechanisms, such as expanding information transmission capacity through signal relaying, and reducing response times of positive feedback loops by increasing initial protein concentrations, may be general design principles for signal transduction.

Methods

Cell Culture

MCF10A cells were purchased from the American Type Culture Collection (ATCC) and were cultured in DMEM/F12 (1:1) medium (Gibco) with 5% horse serum (Gibco), 100 μg/ml of human epidermal growth factor (PeproTech), 10 mg/ml of insulin (Sigma), 10 mg/ml of hydrocortisone (Sigma), 0.5 mg/ml of cholera toxin (Sigma), and 1x penicillin-streptomycin (Gibco). MCF7 cells were purchased from ATCC and cultured in EMEM medium (Gibco) with 10% FBS (Gibco), 10 mg/ml of insulin, and 1x penicillin-streptomycin. A549 cells were purchased from ATCC and were cultured in F12 medium (Corning) with 10% FBS and 1x penicillin-streptomycin. All cells were incubated at 37 °C with 5% CO_2.

TGF-β induce and inhibitor treatment

Cells for TGF-β induction and inhibitor treatment were seeded at ~60-70% confluence without serum starvation. For TGF-β treatment, 4 ng/ml human recombinant TGF-β1 (Cell signaling) was added into culture medium directly. For inhibition experiment, 4 μM of LY2109761 (Selleckchem), 20 μM of GANT61 (Selleckchem), and 10 μM of SB216763 (Selleckchem) were

used to inhibit SMAD, GLI and GSK3, respectively. The medium was changed every day during treatment to keep the reagent concentration constantly. For reproducibility, we used cells within 10^{th} -15^{th} generations, same patches of reagents, serum, and tried to perform each group of experiments (e.g., those in Fig. 1C) together.

Immunofluorescence Microscopy and Data Analysis

Cells were seeded on four-well glass-bottom petri dishes at ~60% confluence overnight and treated with reagents (TGF-β1 and/or inhibitors). Three independent experiments were performed in every treatment. At designated time points, cells were harvested and stained with specific antibodies following procedure modified from the protocols at the Center of Biological Imaging (CBI) in the University of Pittsburgh. In general, cells were washed with DPBS for five minutes for three times followed by 4% formaldehyde fixation for 10 minutes at room temperature. Cells were then washed three times with PBS for five minutes every time. PBS with 0.1% TritonX-100 (PBS_Triton) was used for penetration. BSA of 2% in PBST was used for blocking before staining with antibodies. The first antibodies were diluted by PBST with 1% BSA. Samples were incubated with the first antibodies at 4°C overnight. Then cells were washed three times with 10 minutes for each before being incubated with the secondary antibodies for one hour at room temperature. After antibody incubation, cells were washed with PBS_Triton for five minutes and stained with DAPI (Fisher) for 10 minutes at room temperature. Cells were washed with PBS_Triton for five minutes three times and stored in PBS for imaging.

Photos were taken with Nikon A1 confocal microscopy at CBI. The microscope was controlled by the build-in software, Nikon NIS Elementary. All photos, except the photo for $GSK3^{AA}$ subcellular localization, were taken with plan fluor 40x DIC M/N2 oil objective with 0.75 numerical aperture and 0.72 mm working distance. The scan field were chosen randomly all over

the glass-bottom area. For identifying the $GSK3^{AA}$ subcellular localization, plan apo λ 100x oil objective with 1.45 NA and 0.13 mm WD was used. The 3D model of $GSK3^{AA}$ overlapped with ERC and DAPI were reconstructed from 25 of z-stack images in 11.6 μm and videos were produced also by NIS Element software. To minimize photobleaching, an object field was firstly chosen by fast scan, then the photos were taken at 2014 × 2014 pixel or 4096 × 4096 pixel resolution, for generation large data or for photo presentation, respectively.

CellProfiller was used for cell segregation and initial imaging analysis as what described in Carpenter et.al. [40].

Image Correction. To keep identical background through all images, background correction was performed before further image processing. For each image fluorescent intensities in space without cells were used as local background. Photos that have obviously uneven illumination and background fluorescence were removed from further processing. Otherwise the mean background fluorescent intensity was obtained through averaging over the whole image, and was deducted uniformly from the image.

Image Segmentation. Cell number and position were determined by nuclear recognition with DAPI. The global strategy was used to identify the nuclear shape, and the Otsu algorithm was used for further calculation. Clumped objectives were identified by shape and divided by intensity. Next, using the shrank nuclear shape as seed, cell shape was identified by the Watershed algorithm. For identifying the clusters of $GSK3^{AA}$ formed around a nucleus, the nuclear shape was shrank manually by 3 pixels and used as a new seed to grown the boundary with the watershed method until reaching background intensity level. All parameters were optimized through an iterative process of automatic segmentation and manual inspection.

Image quantification. Averaged fluorescence density and integrated fluorescence intensity were calculated automatically with CellProfiler. The amount of the $GSK3^{AA}$ form was quantified as the sum of intensities of pixels belonging to the cluster formed around a nucleus. Concentrations of all other proteins were quantified by the average pixel intensity within the nucleus or cytosol region of a cell. Next, the

quantified results were examined manually, and those cells with either cell area, nuclear area, or fluorescent intensity beyond five folds of the 95% confidence range of samples from a given treatment were discarded, which account for less than 1% of the cells analyzed. Immunofluorescence data were further processed and plots were generated using customized R codes and Matlab codes. The R package [2], was also used in data analysis.

Quantitative PCR

Cells were seeded in 12-well plastic bottom cell culture plates and treated as described above. Three parallel experiments were performed in every treatment. Total RNA was isolated with the TRIZOL RNA isolation kit (Fisher), and mRNA was reversely transcribed with the RNAscript II kit (ABI). The stem-loop method was used for microRNA reverse transcription. The qPCR system was prepared with the SYBR green qPCR kit with designed primers (Supplementary table 1) and performed on StepOnePlus real-time PCR (ABI).

Immunoprecipitation and silver staining

Immunoprecipitation was performed with SureBeads magnetic beads (Bio-Rad) following a protocol modified from the one provided by the manufacture. We washed beads with PBS with 0.1% Tween 20 (PBS_Tween) for three times, then harvested cells by RIPA (Thermo) with proteinase and phosphatase inhibitor (Roche). Samples were pre-cleaned with 100 µl of suspended Protein G per 450 µl of lysis mixture. Antibodies targeting GSK3 (Cell Signaling), GSK3AA (Santa Cruz), and GSK3D (Santa Cruz) were added into every 100 µl of bead mixture respectively. The mixture was rotated at 4 °C for 3 hours. Beads that were conjugated with antibodies were washed with PBS_Tween. An amount of 100 µl of pre-cleaned lysis buffer was added into conjugated beads and rotated at 4 °C overnight. Targeted proteins were eluded from beads by incubating with 40 µl 1x Laemmli buffer with SDS at 70 °C for 10 minutes. For the samples an amount of 5 µl was used for western blot assay, and an amount of 30 µl was loaded for SDS-PAGE (Bio-Rad) and followed by silver staining (Fisher).

Network reconstruction and coarse-graining

The full network from TGF-β1 to SNAIL1 (Fig. S2A) was generated with IPA (Qiagen®). Specifically, all downstream regulators of TGF-β1 and upstream regulators of SNAIL1 in human, mice and rat were searched and added to the network. Then, direct or indirect relationships between every pair of regulators were searched and added to the network. After obtaining the whole network, regulators that have been reported to be activated later than SNAIL1 were removed. Examination of the network reveals that the network can be further organized into three groups: the TGF-β-SMAD-SNAIL canonical pathway, the TGF-β-GSK3-β-catenin pathway that has the most number of links, and others. We further noticed that GLI1 is a central connector of TGF-β, SMAD, GSK3 and SNAIL1. We performed western blot studies on β-CATENIN and found that neither its concentration nor its location changes significantly before day 3, therefore we removed β-CATENIN from the network. In addition, previous studies report that the SMAD-GLI axis plays important role in TGF-β induced EMT [23]. Therefore we further grouped the network as the SMAD module, the GLI module, and the GSK3 module, as well as the remaining ones that we referred as "Others", and reached the network shown in Fig. 2A. Those molecular species not explicitly specified in Fig. 2A either have their effects implicitly included in the links, for example the link from TGF-β to GSK3, or are included in the links of "Others". This treatment is justified since our various inhibition experiments indeed showed that the three factors we identified affect SNAIL1 expression the most. These "other" species may contribute to snail1 activation at a time later than what considered in this work. Therefore we emphasize the network in Fig. 2A is valid only within the time window we examined, i.e., within three days after TGF-β1 treatment for MCF10A cells.

Acknowledgements

This work was supported by the National Science Foundation [DMS-1462049 to JX], and the Pennsylvania Department of Health (SAP 4100062224). We would like to acknowledge the NIH supported microscopy resources in the Center for Biologic Imaging at University of Pittsburgh, specifically the confocal microscope supported by grant number 1S10OD019973-01.

Figure Caption

Figure 1 Temporal gap exists between SMADs and SNAIL1 in response to TGF-β. (A) Canonical SMAD-dependent pathway for TGF-β activation of SNAIL1. (B) Two-color immunofluorescence (IF) images of pSMAD2/3 and SNAIL1 of MCF10A cells induced by 4 ng/ml TGF-β1 at various time points. The scale bar is 10 μm. Same for other IF images in this paper. (C) Distributions of nuclear pSMAD2/3 and SNAIL1 concentrations quantified from the IF images. Red vertical lines indicate the mean value of the distributions at time 0, and blue vertical lines represent that at 12 h (for pSMAD2/3) or at 48 h (for SNAIL1), respectively. The number on each figure panel is the number of randomly selected cells used for the analysis. Throughout the paper we report fold changes of concentration and amount relative to the mean basal value of the corresponding quantity. (D) Effects of early (added together with TGF-β) and late (48 h after adding TGF-β) pSMAD inhibition on the *SNAIL1* mRNA level. (E) Thorough parameter space search confirmed that with the model in panel A one can fit the pSMAD2/3 dynamics, but not the two-wave SNAIL1 dynamics. The experimental data are shown as violin plots with the medians given by black bars. Solid curves are computational results with parameter sets sampled from the Monte Carlo search, and the red curves are the best-fit results.

Figure 2 Both network analysis and experimental studies revealed GLI1 as a key temporal connector of TGF-β induced SNAIL1 expression. (A) Reconstructed literature-based pathway crosstalks for TGF-β induced SNAIL1 expression. The node "Others" refer remaining SNAIL1 activation pathways that have minor contributions to the time window under study and thus are not explicitly treated. (B) IF images on protein levels of GLI1 (in the free form). Red and blue vertical lines indicate the mean values of the distributions at time 0 and at 48 h, respectively. (C) Distributions of nuclear GLI1 concentrations quantified from the IF images. **(D)** Effects of early (added together with TGF-β) and late (48 h after adding TGF-β) GLI1 inhibition on the *SNAIL1* mRNA level.

Figure 3 TGF-β induced temporal switch between active and inhibitive phosphorylation forms of GSK3 proteins. (A) IF images showed that inhibiting GSK3 enzymatic activity alone increased SNAIL1 accumulation but did not recapitulate TGF-β induced GLI1 nuclear translocation. (B) Quantification of the IF images of MCF10A cells at different time points after TGF-β treatment. Red vertical lines indicate the mean value of the distributions at time 0, and blue vertical lines represent that at 8 h (for $GSK3^{AA}$) or at 12 h (for $GSK3^{D}$), respectively. (C) IF images showing $GSK3^{AA}$ localization at the endoplasmic reticulum center (ERC). (D) Proposed network of the GSK3 module.

Figure 4 The GSK3 phosphorylation switch smoothens the SMAD-GLI1 relay. (A) Proposed expanded network for TGF-β induced SNAIL1 expression. (B) Schematic of a generic positive feedback loop network. Also shown in green is an additional reservoir of the molecules in inactive form (X_I) that can convert quickly into the active form (X) upon stimulation. (C) The

552 response time t_R is sensitive to the initial concentration, $[X]_0$ v.s. $[X]_0 + \Delta[X]_0$. The inlet figure
553 shows the dependence of Δt_R on $[X]_0$ with $\Delta[X]_0$ fixed. (C-D) Box and scattered plots of GSK3
554 inhibition experimental data. On the right panel red points are the center of the scattered plots
555 and each ellipse encloses 97.5% of the data points. Both were drawn with the R package,
556 *car::data.ellipse*.

557

558 **Figure 5 The TGF-β-SNAIL1 network permits detection of TGF-β duration and**
559 **differential responses.** (A) Model predictions that the network generates one or two waves of
560 SNAIL1 depending on TGF-β duration. (B) Single cell protein concentrations quantified from IF
561 images of cells under pulsed and continuous TGF-β treatments. The solid lines divide the space
562 into coarse-grained states with respect to the corresponding mean values without TGF- β
563 treatments (= 1). (C) Schematics of how cells encode information of TGF-β duration through a
564 temporally ordered state space.

565

566 **Figure S1 Supplemental results showing the gap between pSMAD2/3 and SNAIL1**
567 **dynamics.** (A) Scattered plot of the 2D-IF imaging data. (B) Fold change of targeted gene
568 mRNA levels in MCF7 and A549 cells measured with quantitative RT-PCR after TGF-β1
569 treatment. (C) Fold change of targeted gene mRNA levels measured with quantitative RT-PCR
570 after combined TGF-β1 and SMAD2/3 inhibitor LY2109761 treatment. For early inhibition the
571 inhibitor was added at the time of starting TGF-β1 treatment. For late inhibition the inhibitor was
572 added 48 h (for MCF7) and 24 h (for A549) after starting TGF-β1 treatment, respectively. (D)

573 Fold change of miR-34a level in MCF10A cells measured with quantitative RT-PCR after TGF-
574 β1 treatment. (E) Schematic of the parameter space search approach.

575

576 **Figure S2 Supplemental results showing GLI1 as a relay connector between pSMAD2/3**
577 **and SNAIL1.** (A) Network of TGF-β activating SNAIL1 reconstructed with IPA. (B) Scatted
578 plot of measured nuclear GLI1 and SNAIL1 concentrations and the corresponding histogram
579 representation for [nuclear SNAIL1]. The same sets of data of Fig. 2C are used. (C) The model
580 of Fig. 2A with GLI1 reproduces the observed pSMAD2/3-SNAIL1 dynamics. To fit the
581 SNAIL1 dynamics the exact temporal profile of GLI1 is not important except the requirement of
582 its activation after 24 h. (D) Predicted outcome of adding GLI1 inhibitor at different time after
583 TGF-β1 treatment (blue lines). The red line is the predicted dynamics without the inhibitor. (E)
584 Fold change of *GLI1* mRNA levels measured with quantitative RT-PCR at different time points
585 after combined TGF-β1 treatment. (F) Fold change of *SNAIL1* mRNA levels measured with
586 quantitative RT-PCR after combined TGF-β1 and GLI1 inhibitor GANT61 treatment. For early
587 inhibition the inhibitor was added at the time of starting TGF-β1 treatment. For late inhibition
588 the inhibitor was added 48 h (for MCF7) and 24 h (for A549) after starting TGF-β1 treatment,
589 respectively.

590

591 **Figure S3 Supplemental results showing temporal switch between two phosphorylation**
592 **forms of GSK3.** (A) IF images showing the temporal switch between two phosphorylation forms
593 of GSK3. (B) Scattered plots showing correlation between nuclear and cytosol concentrations of
594 $GSK3^{D}$. (C) Immunoprecipitation studies showing two phosphorylation forms do not coexist.
595 Data of two replicas was shown. (D) Silver staining measurement of the relative amount of

596 different GSK3 forms. The right figure shows a representative of three independent replicates. M
597 refers to the marker indicating protein mass.

598

599 **Figure S4. Supplemental results of the full model.** (A) The model of Fig. 4A reproduces the
600 observed GLI1 as well as pSMAD2/3-SNAIL1 dynamics. (B) Examples of regulatory factors
601 having positive feedback loop and reservoir of molecules in inactive form that can be activated
602 by another stimulus. IDPs refer to intrinsically disordered proteins, and some of them are
603 transcription factors, which change into folded form and have higher DNA binding affinity upon
604 binding of cofactors or posttranslational modification. ID1 is a member of the family of
605 inhibitors of DNA binding proteins. (C) Bifurcation diagram showing that the initial
606 concentration boost is small compared to the concentration jump associated with external signal
607 induced switch of cell states. (D-E) Schematics of the early and full GSK3 inhibition
608 experiments.

609

610 **Figure S5** (A) Supplemental model results of pulsed TGF-β treatments with various mutations.
611 (B) Examples of other signaling transduction pathways that share similar motifs as TGF-β,
612 including IL-12, DNA double strand breaking, and LPS, in which extracellular signal is
613 transmitted through a canonical pathway with negative feedbacks and multiple non-canonical
614 pathways, and these pathways crosstalk at multiple points.

615

616 **Supplementary Movie S1: Subcellular localization of GSK3^{AA} (red).** Movies were composed
617 from z-stack imaging.

618 **Supplementary Movie S2: Subcellular localization of GSK3^{AA} (red) overlaid with ERC**

619 **(green) and DAPI (blue, nuclear area).** Movies were composed from z-stack imaging.

620

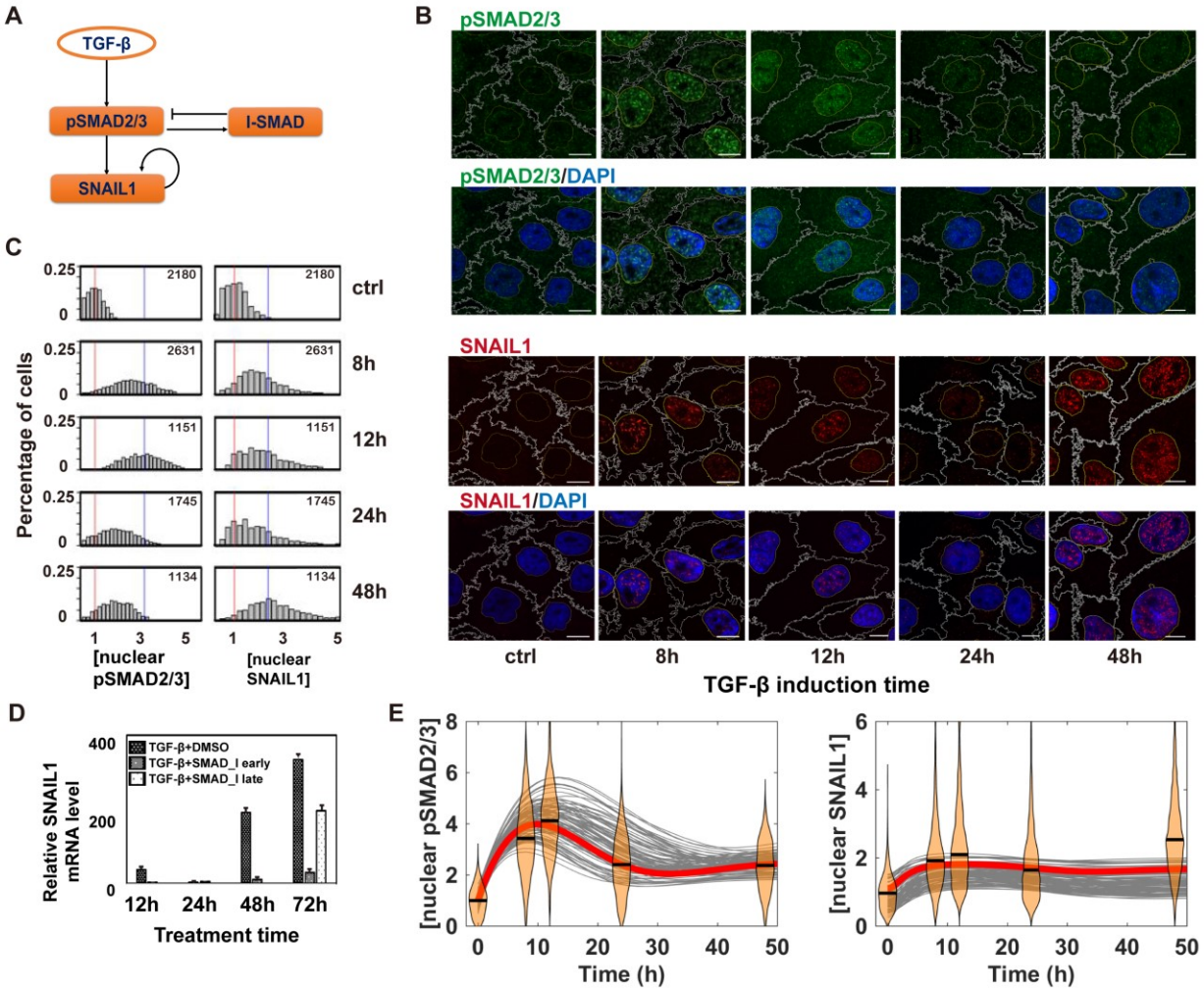

Figure 1

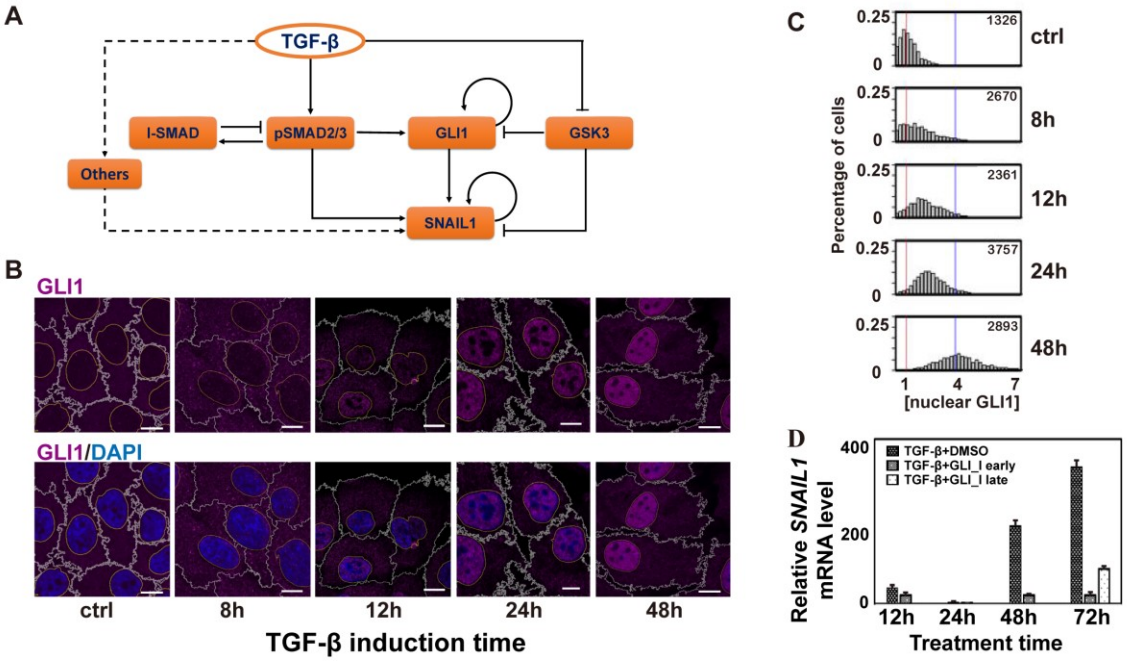

Figure 2

626

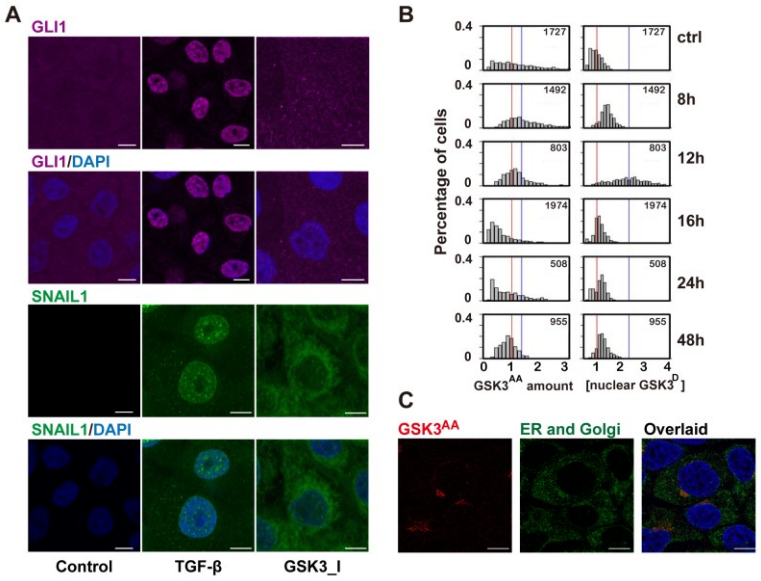

627

628 **Figure 3**

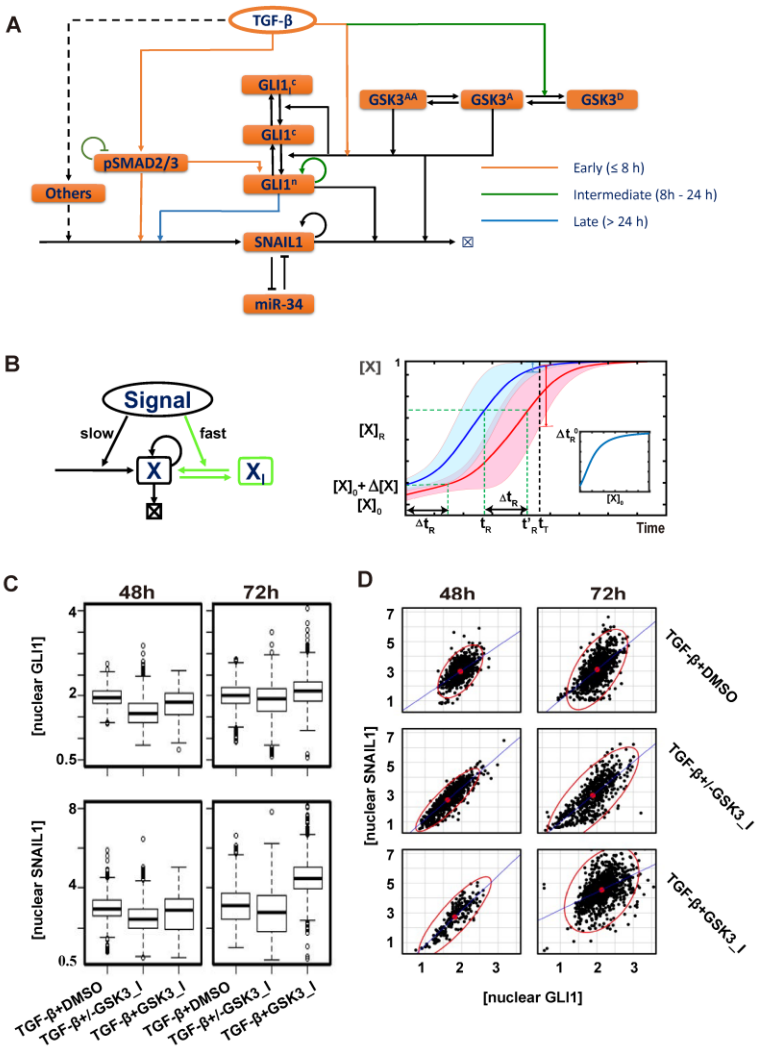

Figure 4

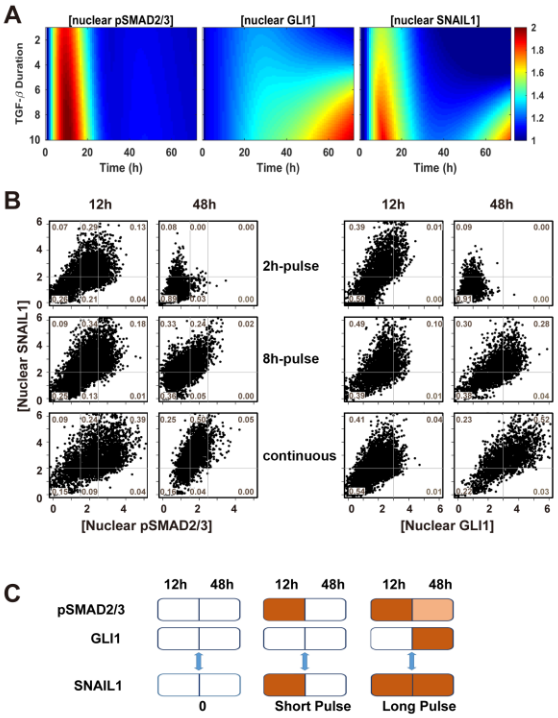

631

632 **Figure 5**

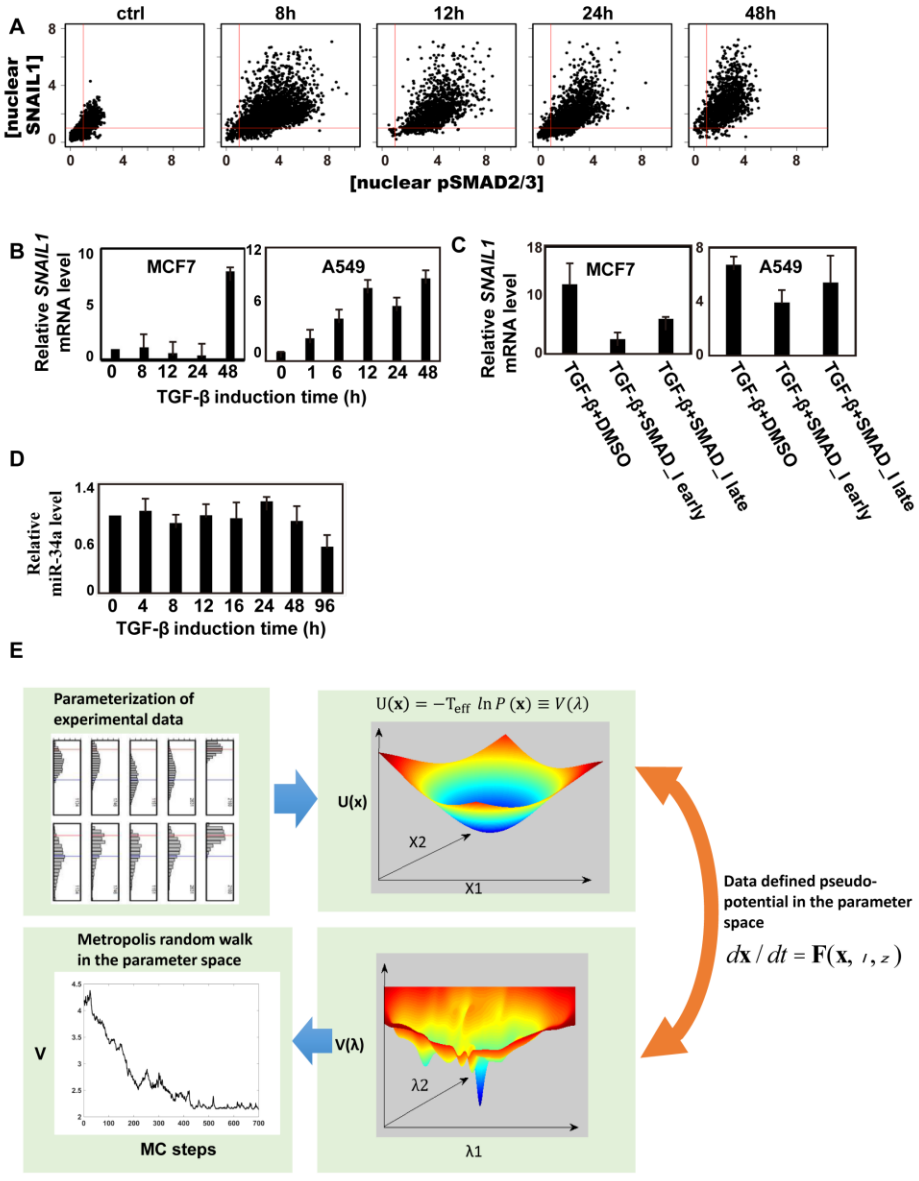

Figure S1

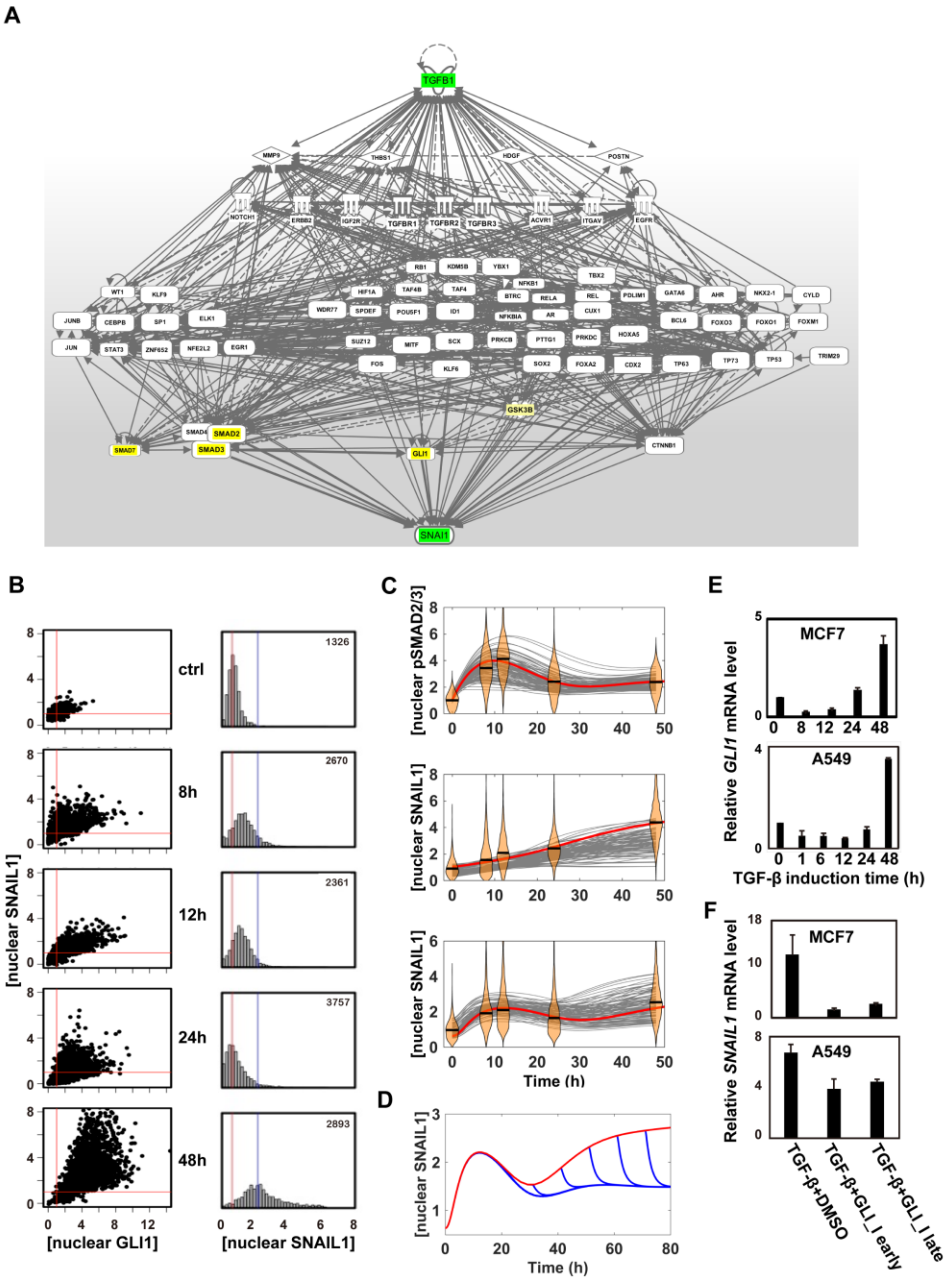

Figure S2

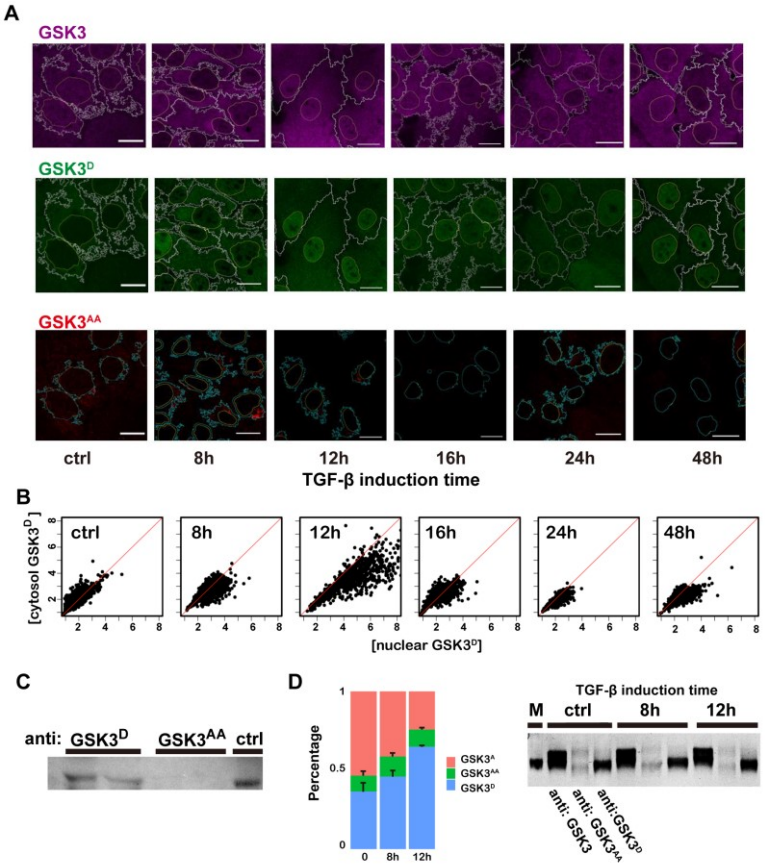

637 .

638 **Figure S3**

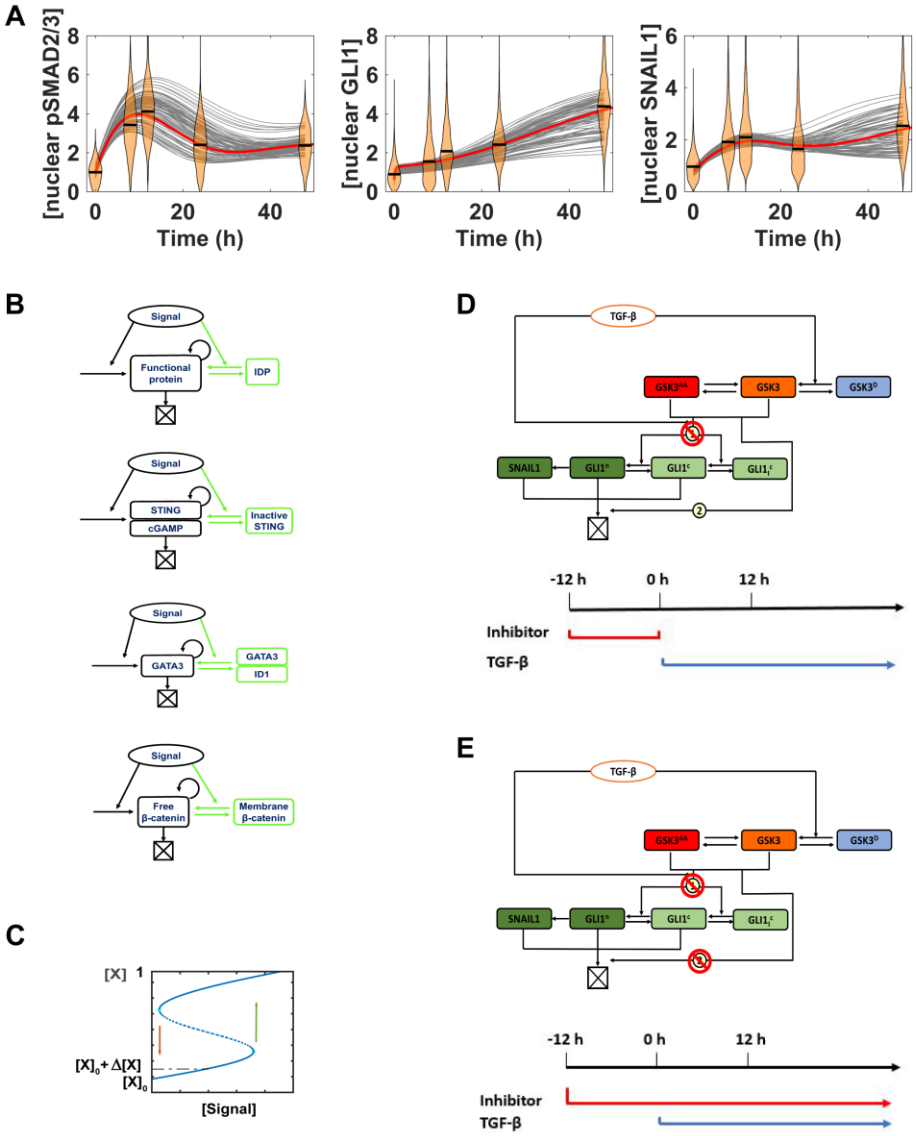

Figure S4

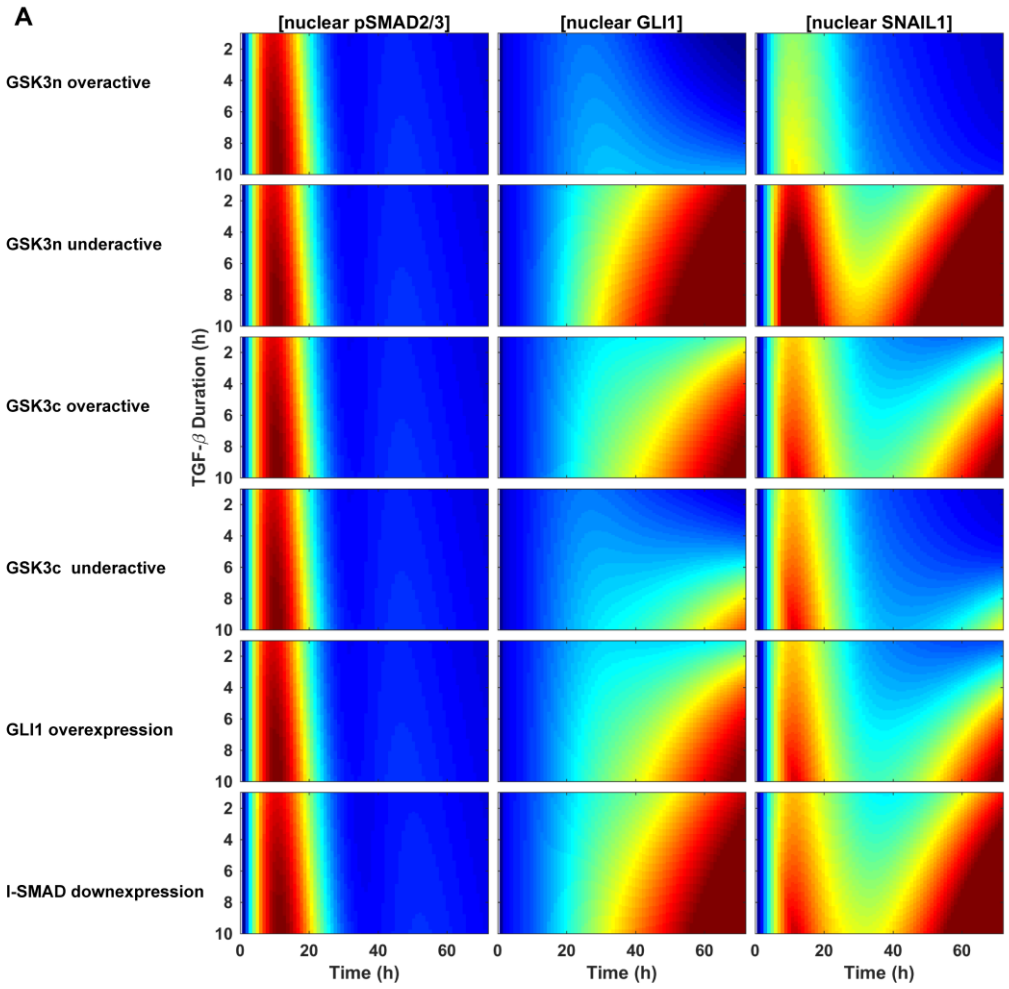

641

642 **Figure S5**

643

644 **Supplementary Materials**

645 **Mathematical modeling**

646 **Canonical TGF-β/pSMAD2/3/SNAILl pathway (Fig. 1A)**

647 We used this ordinary differential equation (ODE) model in Fig. 1 and Fig. S1.

648 **TGF-β/SMAD2/3 module.**

649 $$[\mathrm{Smad}]' = (\mathrm{kp_{smad0}} + \mathrm{kp_{smad}} * \mathrm{TGF}) * \frac{\mathrm{Smad_{all}} - [\mathrm{Smad}]}{\mathrm{Jp_{smad0}} + (\mathrm{Smad_{all}} - [\mathrm{Smad}])} \frac{1}{1 + \frac{\mathrm{Smad_I}}{\mathrm{Jdp_{smad1}}}} - \mathrm{dp_{smad}}$$

650 $$* \frac{[\mathrm{Smad}]}{\mathrm{Jdp_{smad}} + [\mathrm{Smad}]},$$

651 $$[\mathrm{Smad_I}]' = \mathrm{k_{SmadI}} * [\mathrm{Smad}] - \mathrm{kd_{SmadI}} * [\mathrm{Smad_I}],$$

652 where [Smad] and $[\mathrm{Smad_I}]$ are the concentrations of pSMAD2/3 and inhibitory SMAD, respectively.

653 **SNAIL-miR-34 module.** It is expanded from our previous model [20] by considering transcription

654 activation of SNAIL1 by pSMAD2/3 and TGF-β, and degradation of SNAIL1.

655 $$[\mathrm{snail}]'_{\mathrm{n}} = \mathrm{k0_{snail}} + \mathrm{k_{snail0}} * \frac{[\mathrm{Smad}]^2}{\mathrm{J}^2_{\mathrm{snail0}} + [\mathrm{Smad}]^2} \frac{1}{1 + \frac{[\mathrm{SNAIL}]}{\mathrm{J_{snail2}}}} - \mathrm{kd_{snail}} * [\mathrm{snail}] - \mathrm{kd_{SR1}} * [\mathrm{SR1}],$$

656 $$[\mathrm{miR34}]'_{\mathrm{n}} = \mathrm{k0_{34}} + \frac{\mathrm{k_{34}}}{1 + \left(\frac{\mathrm{SNAIL}}{\mathrm{J1_{34}}}\right)^2} - \mathrm{kd_{34}} * [\mathrm{miR34}] - (1 - \lambda_{\mathrm{s}}) * \mathrm{kd_{SR1}} * [\mathrm{SR1}],$$

657 $$[\mathrm{SNAIL}]' = \mathrm{k_{SNAIL}} * [\mathrm{snail}] - \mathrm{kd_{SNAIL}} * [\mathrm{SNAIL}],$$

658 $$[\mathrm{miR34}] = [\mathrm{miR34}]_{\mathrm{t}} - [\mathrm{SR1}],$$

659 $$[\mathrm{snail}] = [\mathrm{snail}]_{\mathrm{t}} - [\mathrm{SR1}],$$

660 $$[\mathrm{SR1}] = \mathrm{Ks} * [\mathrm{snail}] * [\mathrm{miR34}],$$

where [snail], [miR34], [SNAIL], [snail], [SR1] are the concentrations of total *SNAIL1* mRNA, miR-34, SNAIL1 protein, free *SNAIL1* mRNA and miR-34-*SNAIL1* mRNA complex, respectively.

Canonical TGF-β/SMAD/SNAILl pathway with GLI1 (Fig. S2)

Taking into account the GLI1 self-activation and GLI1 mediated expression of *SNAIL1* mRNA, we added another ODE for GLI1 and revised the ODE of *SNAIL1* mRNA.

$$[\mathrm{GLI}]_n' = k_{gli0} + k_{gli1} * \frac{[\mathrm{Smad}]^2}{J_{gli1}^2 + [\mathrm{Smad}]^2} + k_{gli2} * \frac{[\mathrm{GLI}]_n{}^2}{[\mathrm{GLI}]n^2 + J_{gli2}^2} - d_{gli} * [\mathrm{GLI}]_n,$$

$$[\mathrm{snail}]_t' = k0_{snail} + \left(k_{snail0} * \frac{[\mathrm{Smad}]^2}{J_{snail0}^2 + [\mathrm{Smad}]^2} + k_{snail1} * \frac{[\mathrm{GLI}]_n{}^m}{[\mathrm{GLI}]_n{}^2 + J_{snail1}^m}\right) \frac{1}{1 + \frac{[\mathrm{SNAIL}]}{J_{snail2}}} - kd_{snail} * [\mathrm{snail}] - kd_{SR1} * [\mathrm{SR1}],$$

where $[\mathrm{GLI}]_n$ is the concentration of nuclear GLI1. We used this ODE model to generate results in Fig. S2.

Model for the GSK3/GLI module (Fig. 4A)

Since the process involves many steps and a detailed model would require many parameters to determine, instead we used two phenomenological time-dependent functions to qualitatively mimic the dynamics of the enzyme activities of cytosol GSK3 and nuclear GSK3 we experimentally measured,

$$[\mathrm{GSK}]_c(t) = k_{GSKc} * \mathrm{TGF} * \left(1 - \exp\left(-\frac{t}{a1}\right)\right) * \exp\left(-\frac{t - b1}{a1}\right),$$

$$[\mathrm{GSK}]_n(t) = 1 - k_{GSKn} * \mathrm{TGF} * \left(1 - \exp\left(-\frac{t}{a2}\right)\right) * \left(\exp\left(-\frac{t - b2}{a2}\right)\right).$$

Furthermore, the basal pool of cytosol GLI1 is considered, which is by sequestered in the cytosol by Sufu but could translocate to the nuclear after Sufu is inactivated by the cytosol enzyme GSK3 activity. We used a revised ODE of nuclear GLI1 concentration derived with the quasi-equilibrium approximation (see below)

681 $$[\mathrm{GLI}]_t' \approx k_{gli0} + k_{gli1} * \frac{[\mathrm{Smad}]^2}{J_{gli1}^2 + [\mathrm{Smad}]^2} + k_{gli2} * \frac{[\mathrm{GLI}]_n^{nm}}{[\mathrm{GLI}]_n^{m} + J_{gli2}^m} - d_{gli} * [\mathrm{GLI}]_n * [\mathrm{GSK}]_n;$$

682 $$[\mathrm{GLI}]_n = \frac{[\mathrm{GSK}]_c + K1}{(K3+1)[\mathrm{GSK}]_c + K1 + K4} [\mathrm{GLI}]_t$$

683 **Derivation of GLI ODE,**

684 We assumed the quasi-equilibrium approximation for the GLI nuclear and cytosol shuttling, the GSK3

685 regulated binding/unbinding between Sufu and GLI in the cytosol, and obtained the following equations,

686 $$K2 * [\mathrm{GLI}]_c * [\mathrm{Sufu}] = (K1 + [\mathrm{GSK}]_c) * [\mathrm{GLIsufu}],$$

687 $$[\mathrm{GLIsufu}] = \mathrm{Sufu}_{max} - [\mathrm{Sufu}]$$

688 Thus we have

689 $$[\mathrm{GLIsufu}] = \mathrm{Sufu}_{max} - (K1 + [\mathrm{GSK}]_c) * \frac{[\mathrm{GLIsufu}]}{K2 * [\mathrm{GLI}]_c}$$

690 That is,

691 $$[\mathrm{GLIsufu}] = \frac{1}{1 + \frac{(K1 + [\mathrm{GSK}]_c)}{K2 * [\mathrm{GLI}]_c}} \mathrm{Sufu}_{max}$$

692 Also we have $[\mathrm{GLI}]_c = K3 * [\mathrm{GLI}]_n$, thus

693 $$[\mathrm{GLIsufu}] = \frac{K3 * K2 * [\mathrm{GLI}]_n}{K3 * K2 * [\mathrm{GLI}]_n + (K1 + [\mathrm{GSK}]_c)} \mathrm{Sufu}_{max}$$

694 The total level of GLI1 is the sum of the three forms, GLISufu, GLI_c and GLI_n,

695 $$[\mathrm{GLI}]_t = [\mathrm{GLI}]_c + [\mathrm{GLI}]_n + [\mathrm{GLIsufu}] = \left(K3 * [\mathrm{GLI}]_n + [\mathrm{GLI}]_n + \frac{K2 * K3 * [\mathrm{GLI}]_n}{K3 * K2 * [\mathrm{GLI}]_n + (K1 + [\mathrm{GSK}]_c)} \mathrm{Sufu}_{max}\right).$$

696 Thus, we obtained the relation among $[GLI]_n$, $[GLI]_t$ and $[\mathrm{GSK}]_c$

697 $$[\mathrm{GLI}]_n = f(GSK_c, [\mathrm{GLI}]_t),$$

The total concentration of GLI1 is given by,

$$[GLI]_t' = k_{gli0} + k_{gli1} * \frac{[Smad]^2}{J_{gli1}^2 + [Smad]^2} + k_{gli2} * \frac{[GLI]_n{}^m}{[GLI]_n{}^m + J_{gli2}^m} - d_{gli} * [GLI]_c * [GSK]_c - d_{gli} * [GLI]_n * [GSK]_n.$$

Given that our data shows that $[GLI]_c$ is low throughout the process, we neglected the degradation term of $[GLI]_c$,

$$[GLI]_t' \approx k_{gli0} + k_{gli1} * \frac{[Smad]^2}{J_{gli1}^2 + [Smad]^2} + k_{gli2} * \frac{[GLI]_n{}^m}{[GLI]_n{}^m + J_{gli2}^m} - d_{gli} * [GLI]_n * [GSK]_n$$

TGF-β pulse

Since TGF-β1 can enter to cells through endocytosis, washing the extracellular TGF-β1 does not stop the signaling immediately. Therefore, we modeled the effective TGF-β1 concentration by the following equation,

$$[TGF](t) = TGF_0 * \exp\big(-d_{tgf} * (t - TGF_{Duration}) * Heaviside(t - TGF_{Duration})\big).$$

Full model

By considering all the modules, the full model is as following,

$$[Smad]' = (kp_{smad0} + kp_{smad} * [TGF]) * \frac{Smad_{all} - [Smad]}{Jp_{smad0} + (Smad_{all} - [Smad])} \frac{1}{1 + \frac{[Smad_I]}{Jdp_{smad1}}} - dp_{smad} * \frac{[Smad]}{Jdp_{smad} + [Smad]},$$

$$[Smad_I]' = k_{SmadI} * [Smad] - kd_{SmadI} * [Smad_I],$$

$$[GLI]_t' = k_{gli0} + k_{gli1} * \frac{Smad23^2}{J_{gli1}^2 + Smad23^2} + k_{gli2} * \frac{[GLI]_n{}^m}{[GLI]_n{}^m + J_{gli2}^m} - d_{gli} * [GLI]_c * [GSK]_c - d_{gli} * [GLI]_n * [GSK]_n,$$

$$[\text{snail}]_t' = k0_{snail} + \left(k_{snail0} * \frac{[Smad]^2}{J_{snail0}^2 + [Smad]^2} + k_{snail1} * \frac{[GLI]_n{}^m}{[GLI]_n{}^m + J_{snail1}^m}\right) \frac{1}{1 + \frac{[SNAIL]}{J_{snail2}}} - kd_{snail} * [\text{snail}] -$$

$$kd_{SR1} * [SR1],$$

$$[\text{miR34}]_n' = k0_{34} + \frac{k_{34}}{1 + \left(\frac{SNAIL}{J1_{34}}\right)^2} - kd_{34} * [\text{miR34}] - (1 - \lambda_s) * kd_{SR1} * [SR1],$$

$$[SNAIL]' = k_{SNAIL} * [\text{snail}] - kd_{SNAIL} * [SNAIL] * [GSK]_n,$$

$$[GSK]_c(t) = k_{GSKc} * [TGF] * \left(1 - \exp\left(-\frac{t}{a1}\right)\right) * \exp\left(-\frac{t - b1}{a1}\right),$$

$$[GSK]_n(t) = 1 - k_{GSKn} * [TGF] * \left(1 - \exp\left(-\frac{t}{a2}\right)\right) * \left(\exp\left(-\frac{t - b2}{a2}\right)\right),$$

$$[GLI]_n = f([GSK]_c, [GLI]_t)$$

$$[\text{miR34}] = [\text{miR34}]_t - [SR1],$$

$$[\text{snail}] = [\text{snail}]_t - [SR1],$$

$$[SR1] = Ks * [\text{snail}] * [\text{miR34}].$$

We used this ODE model to generate results in Fig. 5 and Fig. S5A.

Parameter space searching

Step 1: Calculate single cell distributions of experimental observables. We calculated histograms of the distributions from the single cell experimental data. Suppose that we have N observables measured in M time points, we have an $N \times M$ dimensional distribution of the data. Since we used fixed cells and we had no information on the temporal correlation, we treated the distributions from different time points as independent, *i.e.*, $P = \prod_{i=1}^{M} P_i$.

Step 2: Define pseudo-potentials from the parameterized distribution. We defined a pseudo-scalar-potential function $U(\mathbf{x}_1, \mathbf{x}_2, .., \mathbf{x}_M) = -T_{eff}\,(lnP - lnP_{max})$. The constant T_{eff} is an effective

temperature, which we chose $T_{eff} = 1$. The constant term $lnPmax$ sets the potential to be zero at the peak position of the distribution, and does not affect the parameter space search results. This pseudo-potential is just an auxiliary scalar function for the following application of the Metropolis algorithm. If a mathematical model can faithfully describe the system dynamics, with given initial conditionals and non-adjustable parameter set of $\boldsymbol{\zeta}$, we should be able to find distributions of the parameter set $\boldsymbol{\lambda}$ (to take into account cell-to-cell heterogeneity), and generate the corresponding distributions of $(\mathbf{x}_1, \mathbf{x}_2, .., \mathbf{x}_\mathrm{M})$ to reproduce U. That is, for a specific set of $\boldsymbol{\lambda}$, $\mathbf{x}_\mathrm{i} = \mathbf{x}_\mathrm{i}(\mathbf{x}_0; \boldsymbol{\lambda}, \boldsymbol{\zeta}), \mathrm{i} = 1, \ldots M$, and $U(\mathbf{x}_1, \mathbf{x}_2, .., \mathbf{x}_\mathrm{M}) \equiv V(\boldsymbol{\lambda})$. Unlike U, the function form of V can be very complex, but fortunately we do not need to know its explicit function form to perform the following Metropolis sampling.

Step 3: Obtain model parameter distributions that reproduce the distributions of experimental observables.

Now it is clear why we define the pseudo-potential. We performed Monte Carlo random walks along the pseudo-potential V in the $\boldsymbol{\lambda}$ space using the Metropolis algorithm, just as how the algorithm is typically applied along real physical potentials. At each step with a set of $\boldsymbol{\lambda}$, we generated a trial move $\boldsymbol{\lambda}' = \boldsymbol{\lambda} + \boldsymbol{\delta\lambda}$. We propagated the ODEs to obtain $V(\boldsymbol{\lambda})$ and $V(\boldsymbol{\lambda}')$, then use the Metropolis criteria to decide whether to accept the new move. If $V(\boldsymbol{\lambda}') \leq V(\boldsymbol{\lambda})$ accept this step and update the parameter set $\boldsymbol{\lambda} = \boldsymbol{\lambda}'$. If $V(\boldsymbol{\lambda}') > V(\boldsymbol{\lambda})$, accept this step with a probability $\exp(-(V(\boldsymbol{\lambda}') - V(\boldsymbol{\lambda}))/T)$, with $T = 1$.

In our model, there is no feedback between the SMAD2/3 module and the SNAIL1/miR-34 module, thus we used a two-step to searching the parameter space for the TGF-β/SMAD2/3 module,

1. Search the parameter space (nine parameters) in the SMAD2/3 module;
2. Search the parameter space (six parameters) for the SNAIL1/miR-34 module based on the 50 samples of good-fit parameter set of the SMAD2/3 module from step 1.

In step 2 some of the parameters in the SNAIL1/miR-34 module were fixed and used as a well-trained parameter set from our previous work [20]. Instead only six new parameters that connect the module SMAD2/3 and module SNAIL1/miR-34 were considered in the parameter space searching.

When the GLI1 module was included, we again used the fact that there is no feedback between the SMAD2/3 module and the GLI1 module, and used a three-step searching procedure to reduce the computational efforts,

1. Search the parameter space (nine parameters) for the SMAD2/3 module;
2. Search the parameter space (seven parameters) for the GLI1 module;
3. Search the parameter space (six parameters) for the SNAIL1/miR-34 module based on the 50 samples of good-fit parameter set of the SMAD2/3 module the GLI1 module from step 1-2.

Parameter change in various over-expression/down-expression or over-active/down-active conditions (Fig. S5)

To produce the results in Fig. S5A, a 1.2-fold change of k_{gli0} is used in the case of GLI1 over-expression, a 0.8-fold change of k_{smadi} in the case of I-SMAD down-regulation. There is 0.8-fold change of k_{gskn} in the case of over-active cytosol GSK3, 1.2-fold change of k_{gskn}in the case of under-active cytosol GSK3. Similarly, there is 1.2-fold change of k_{gskc} in the case of over-active nuclear GSK3, and 0.5-fold change of k_{gskc} in the case of under-active nuclear GSK3.

774 **Supplementary Table 1. Primer list**

Primers	Sequence	References
SNAIL1_QRT_F	ATCGGAAGCCTAACTACAGCGA	41
SNAIL1_QRT_R	CACGCCTGGCACTGGTACTTCT	
GLI1_QRT_F	CTCCCTCGTAGCTTTCATCAAC	
GLI1_QRT_F	GTGCTCGCTGTTGATGTGGTG	
GAPDH_QRT_F	ACCACAGTCCATGCCATCAC	41
GAPDH_QRT_F	TCCACCACCCTGTTGCTGTA	
Stem_loop_Uni	GTCGTATCCAGTGCAGGGTCCGAGGTATTCGCACTGGATACGAC	42
miR-34a-5p_SL	GTCGTATCCAGTGCAGGGTCCGAGGTATTCGCACTGGATACGACACAACC	
Universal_primer	CCAGTGCAGGGTCCGAGGTA	
miR-34a-5p_RT	CACGCATGGCAGTGTCTTAGC	

775

776

777 **Supplementary Table 2. The Parameters values of the best fit of the full model.**

Parameter	Description	Value
TGF-β/SMAD2/3 module		
kp_smad0	Basal activation rate of SMAD2/3	1.5778 μM/hr
kp_smad	TGF-β dependent activation rate of SMAD2/3	0.2675 μM/hr
$Smad_{all}$	The total level of SMAD2/3	27.5377 μM
dp_smad	Deactivation rate of SMAD2/3	1.4833 μM/hr
Jp_smad0	Michaelis constant of SMAD2/3 activation	0.4198 μM
Jdp_smad	Michaelis constant of SMAD2/3 deactivation	0.3639 μM
Jp_smad1	Michaelis constant of SMAD-I mediated inhibition of SMAD2/3 activation	0.8326 μM
k_smadi	Expression rate of inhibitory SMAD	0.0254 μM/hr
kd_smadi	Degradation rate of inhibitory SMAD	0.0710 μM/hr
GSK3 /GLI1 module		
k_GSKc	The activation rate of cytosol $GSK3^{AA}$ enzyme activity	1/hr
k_GSKn	The deactivation rate of nuclear GSK3 enzyme activity	0.25/hr
a1	Constant a of cytosol GSK3 enzyme activity	10
b1	Constant b of cytosol GSK3 enzyme activity	10
a2	Constant a of nuclear GSK3 enzyme activity	20
b2	Constant b of nuclear GSK3 enzyme activity	20
k_gli0	Basal transcription rate of *gli1*	0.0003 μM/hr
k_gli1	SMAD2/3-dependent transcription rate of *gli1*	0.0453 μM/hr
k_gli2	GLI1-dependent transcription rate of *gli1*	0.2288 μM/hr

d_gli	Degradation rate of GLI1	0.0166 /hr
J_gli1	Michaelis constant of SMAD2/3 -dependent transcription of *gli1*	0.7563 μM
J_gli2	Michaelis constant of GLI1-dependent transcription of *gli1*	2.4192 μM
SNAIL1/miR-34 module		
$k0_{snail}$	Basal transcription rate of *snail1*	0.0034 μM/hr
k_{snail0}	SMAD2/3-dependent transcription rate of *snail1*	1.3942 μM/hr
k_{snail1}	GLI1-dependent transcription rate of *snail1*	43.5453 μM/hr
J_{snail0}	Michaelis constant of SMAD2/3-dependent *snail1* transcription	0.7522 μM
J_{snail1}	Michaelis constant of GLI1-dependent *snail1* transcription	7.2215 μM
J_{snail1}	Michaelis constant of SNAIL1-dependent *snail1* transcription inhibition	0.2012 μM
kd_{snail}	Degradation rate of *SNAIL1* mRNA	0.09 /hr
kd_{SR}	Degradation rate of miR34-*SNAIL1* complex	0.9 /hr
k_{SNAIL}	Translation rate of *SNAIL1* mRNA	17 μM/hr
kd_{SNAIL}	Degradation rate of SNAIL1	1.66 /hr
$k0_{34}$	Basal production rate of miR-34	0.0012 μM/hr
k_{34}	Production rate of miR-34	0.012 μM/hr
$J1_{34}$	Michaelis constant of SNAIL1-dependent inhibition of miR-34 production	0.15 μM
kd_{34}	Degradation rate of miR-34	0.035 /hr
K_s	Affinity constant of miR-34 and *SNAIL1* mRNA	100 /μM
λs	Recycle ratio of miR-34	0.5

The parameters shaded are searched with our algorithm.

Reference

1. Albeck, J.G., Mills, G.B. & Brugge, J.S. Frequency-modulated pulses of ERK activity transmit quantitative proliferation signals. *Mol Cell* **49**, 249-261 (2013).
2. English, J.G. *et al.* MAPK feedback encodes a switch and timer for tunable stress adaptation in yeast. *Sci Signal* **8**, ra5 (2015).
3. Fu, Y. *et al.* Reciprocal encoding of signal intensity and duration in a glucose-sensing circuit. *Cell* **156**, 1084-1095 (2014).
4. Kholodenko, B.N. Cell-signalling dynamics in time and space. *Nat Rev Mol Cell Biol* **7**, 165-176 (2006).
5. Nathan, C. Points of control in inflammation. *Nature* **420**, 846-852 (2002).
6. Massagué, J. TGFβ signalling in context. *Nat Rev Mol Cell Biol* **13**, 616-630 (2012).
7. Massagué, J. How cells read TGF-β signals. *Nat Rev Mol Cell Biol* **1**, 169-178 (2000).
8. Borthwick, L.A. & Wynn, T.A. IL-13 and TGF-β1: core mediators of fibrosis. *Curr Pathobiol Rep* **3**, 273-282 (2015).
9. Lamouille, S., Xu, J. & Derynck, R. Molecular mechanisms of epithelial-mesenchymal transition. *Nat Rev Mol Cell Biol* **15**, 178-196 (2014).
10. Wu, M.Y. & Hill, C.S. Tgf-β superfamily signaling in embryonic development and homeostasis. *Dev Cell* **16**, 329-343 (2009).
11. Moses, H.L., Roberts, A.B. & Derynck, R. The discovery and early days of TGF-β: A historical perspective. *Cold Spring Harb Perspect Biol* **8**, a021865 (2016).
12. Fabregat, I., Fernando, J., Mainez, J. & Sancho, P. TGF-β signaling in cancer treatment. *Curr Pharm Des* **20**, 2934-2947 (2014).
13. Colak, S. & ten Dijke, P. Targeting TGF-β signaling in cancer. *Trends in Cancer* **3**, 56-71 (2017).
14. Vizán, P. *et al.* Controlling long-term signaling: receptor dynamics determine attenuation and refractory behavior of the TGF-β pathway. *Sci Signal* **6**, ra106 (2013).
15. Warmflash, A. *et al.* Dynamics of TGF-β signaling reveal adaptive and pulsatile behaviors reflected in the nuclear localization of transcription factor Smad4. *Proc Natl Acad Sci USA* **109**, E1947-1956 (2012).
16. Zi, Z. *et al.* Quantitative analysis of transient and sustained transforming growth factor-β signaling dynamics. *Mol Syst Biol* **7**, 492 (2011).
17. Xu, J., Lamouille, S. & Derynck, R. TGF-β-induced epithelial to mesenchymal transition. *Cell Res* **19**, 156-172 (2009).
18. Thuault, S. *et al.* HMGA2 and Smads co-regulate SNAIL1 expression during induction of epithelial-to-mesenchymal transition. *J Biol Chem* **283**, 33437-33446 (2008).
19. Schmierer, B., Tournier, A., Bates, P. & Hill, S. Mathematical modeling identifies Smad nucleocytoplasmic shuttling as a dynamic signal-interpreting system. *Proc Natl Acad Sci USA* **105**, 6608-6613 (2008).
20. Zhang, J. *et al.* TGF-β-induced epithelial-to-mesenchymal transition proceeds through stepwise activation of multiple feedback loops. *Sci Signal* **7**, ra91-ra91 (2014).
21. Aomatsu, K. *et al.* TGF-β induces sustained upregulation of SNAI1 and SNAI2 through Smad and non-Smad pathways in a human corneal epithelial cell line. *Invest Ophthalmol Vis Sci* **52**, 2437-2443 (2011).
22. Dennler, S. *et al.* Induction of sonic hedgehog mediators by transforming growth factor-β: Smad3-dependent activation of Gli2 and Gli1 expression in vitro and in vivo. *Cancer Res* **67**, 6981-6986 (2007).

23. Javelaud, D. *et al.* TGF-β/SMAD/GLI2 signaling axis in cancer progression and metastasis. *Cancer Res* **71**, 5606-5610 (2011).
24. Steinway, S.N. *et al.* Network modeling of TGFβ signaling in hepatocellular carcinoma epithelial-to-mesenchymal transition reveals joint sonic hedgehog and Wnt pathway activation. *Cancer Res* **74**, 5963-5977 (2014).
25. Schlessinger, K. & Hall, A. GSK-3β sets Snail's pace. *Nat Cell Biol* **6**, 913-915 (2004).
26. Mizuarai, S., Kawagishi, A. & Kotani, H. Inhibition of p70S6K2 down-regulates Hedgehog/GLI pathway in non-small cell lung cancer cell lines. *Mol Cancer* **8**, 44 (2009).
27. Hughes, K., Nikolakaki, E., Plyte, S.E., Totty, N.F. & Woodgett, J.R. Modulation of the glycogen synthase kinase-3 family by tyrosine phosphorylation. *EMBO J.* **12**, 803-808 (1993).
28. Meares, G.P. & Jope, R.S. Resolution of the nuclear localization mechanism of glycogen synthase kinase-3: functional effects in apoptosis. *J Biol Chem* **282**, 16989-17001 (2007).
29. Takenaka, K., Kise, Y. & Miki, H. GSK3β positively regulates Hedgehog signaling through Sufu in mammalian cells. *Biochem Bioph Res Co* **353**, 501-508 (2007).
30. Cole, A., Frame, S. & Cohen, P. Further evidence that the tyrosine phosphorylation of glycogen synthase kinase-3 (GSK3) in mammalian cells is an autophosphorylation event. *Biochem J* **377**, 249 (2004).
31. Selimkhanov, J. *et al.* Accurate information transmission through dynamic biochemical signaling networks. *Science* **346**, 1370-1373 (2014).
32. Cheong, R., Rhee, A., Wang, C.J., Nemenman, I. & Levchenko, A. Information Transduction Capacity of Noisy Biochemical Signaling Networks. *Science* **334**, 354-358 (2011).
33. Shirakihara, T., Saitoh, M. & Miyazono, K. Differential regulation of epithelial and mesenchymal markers by δEF1 proteins in epithelial mesenchymal transition induced by TGF-β. *Mol Biol Cell* **18**, 3533-3544 (2007).
34. Fuxe, J., Vincent, T. & Garcia de Herreros, A. Transcriptional crosstalk between TGFβ and stem cell pathways in tumor cell invasion: role of EMT promoting Smad complexes. *Cell Cycle* **9**, 2363-2374 (2010).
35. Aberger, F. & Ruiz, I.A.A. Context-dependent signal integration by the GLI code: the oncogenic load, pathways, modifiers and implications for cancer therapy. *Semin Cell Dev Biol* **33**, 93-104 (2014).
36. Doble, B.W. & Woodgett, J.R. GSK-3: tricks of the trade for a multi-tasking kinase. *J Cell Sci* **116**, 1175-1186 (2003).
37. Kretschmer, A. *et al.* Differential regulation of TGF-β signaling through Smad2, Smad3 and Smad4. *Oncogene* **22**, 6748-6763 (2003).
38. Franco, D.L. *et al.* Snail1 suppresses TGF-β-induced apoptosis and is sufficient to trigger EMT in hepatocytes. *J. Cell. Sci.* **123**, 3467-3477 (2010).
39. Fabian, S.L. *et al.* Hedgehog-Gli pathway activation during kidney fibrosis. *Am J Pathol* **180**, 1441-1453 (2012).
40. Carpenter, A.E. *et al.* CellProfiler: image analysis software for identifying and quantifying cell phenotypes. *Genome Biol* **7**, R100 (2006).
41. Zheng, X. *et al.* The transcription factor GLI1 mediates TGFβ1 driven EMT in hepatocellular carcinoma via a SNAI1-dependent mechanism. *PloS One* **7**, e49581 (2012).
42. Kramer, M.F. Stem-Loop RT-qPCR for miRNAs. *Curr Protoc Mol Biol*, 15.10. 11-15.10. 15 (2011).